Ceramics International 51 (2025) 46593–46603

Contents lists available at ScienceDirect

Ceramics International

journal homepage: www.elsevier.com/locate/ceramint

Degradation mechanisms of magnesia-carbon refractories in radiation heat-affected wall of steel electric arc furnace

Kianoosh Kaveh [a], Mansoor Barati [b], Mohammad Jahazi [a], Elmira Moosavi-Khoonsari [a,*]

[a] Department of Mechanical Engineering, École de Technologie Supérieure (ÉTS), 1100 Notre-Dame Street West, Montréal, QC, H3C 1K3, Canada
[b] Department of Materials Science & Engineering, University of Toronto, 184 College Street, Toronto, ON, M5S 3E4, Canada

ARTICLE INFO

Handling Editor: Dr P. Vincenzini

Keywords:
Magnesia-carbon refractories
Electric arc furnace
Degradation mechanisms
Porous network development
Thermal volume expansion

ABSTRACT

This study investigates the mechanisms underlying microstructural deterioration in processed MgO-C refractories from the radiation heat-affected wall of a steel EAF. X-ray tomography and scanning electron microscopy with energy-dispersive spectroscopy were employed to identify the thermally activated chemical, physical, and mechanical degradation phenomena and to evaluate their impact on microstructural evolution during the process. The results reveal that degradation is primarily driven by the development of a porous network surrounding coarse MgO grains (>~3 mm), with a strong correlation observed between MgO grain size and damage evolution. Larger grains tend to promote more extensive porous networks, which in turn facilitate oxygen ingress and accelerate carbon oxidation. The pronounced mismatch in thermal expansion coefficients between MgO grains and the carbon matrix contributes to crack formation and grain detachment. These findings provide deeper insight into the failure mechanisms of MgO-C refractories and inform strategies for optimizing refractory design to extend service life and enhance performance.

1. Introduction

The electric arc furnace (EAF) steelmaking route accounted for approximately 20 % of global steel production in the year 2020 and is projected to increase to 27 % by the year 2030 in the net-zero emission 2050 scenarios [1]. The utilization of recycled scrap and direct reduced iron (DRI) as the production feed and using electricity as the energy source instead of fossil fuels contributes to more environmentally friendly steel production and reduces the industry's carbon footprint [2,3]. Although the EAF route is a well-established practice, it is still faced with challenges arising from the harsh nature of the process and the ongoing demand for improvement in the quality and service life and cost-effectiveness of the production system components. One of the most significant challenges in EAF steelmaking is the failure of refractory lining, which can lead to furnace downtime, production loss, and, in extreme cases, jeopardize the safety of the operation [4].

Carbon-bonded magnesia (MgO-C) refractories are widely employed for lining the sidewalls of EAFs due to their cost-effectiveness, high refractoriness, durability, and thermal shock resistance. However, the carbon matrix within these refractories, varying from 4–5 to 30–35 wt% [4], is highly susceptible to oxidation damage, resulting in deterioration and profile reduction over extended periods [5–7]. Incorporating different types of antioxidant particles, such as metals (Al, Si, Fe), carbides (Cr_7C_3, Ti_3AlC_2, Ti_3SiC_2), and borides (MgB_2, $Mg_2B_2O_5$, Zr_2B), into the carbon matrix has been a primary focus to improve the oxidation resistance of these refractories [5,8–12]. Over the past two decades, advancements in nanomaterials and advanced ceramics have also spurred interest in applying carbon nanotubes and other carbon or ceramic reinforcements in this field [13].

The kinetics of carbon oxidation in the MgO-C refractory matrix are critical for understanding deterioration mechanisms and evaluating in-process lifetime. Several studies have investigated oxidation kinetics in MgO-C refractories using various models and experimental conditions [6,14–17]. These studies have provided valuable insights into the mechanisms driving oxidation at different temperatures and carbon contents. Faghihi-Sani and Yamaguchi [6] investigated oxidation kinetics in the 1000–1200 °C range under airflow for up to 8 h. They measured mass loss and cross-sectional reduction in cylindrical samples and utilized a shrinking core model to describe the oxidation process. However, the mass loss model was validated only over a limited temperature range below the typical range in the actual process, and the effect of antioxidants was not considered.

* Corresponding author.
E-mail addresses: Kianoosh.kaveh.1@ens.etsmtl.ca (K. Kaveh), Mansoor.barati@utoronto.ca (M. Barati), Mohammad.Jahazi@etsmtl.ca (M. Jahazi), Elmira.moosavi@etsmtl.ca (E. Moosavi-Khoonsari).

https://doi.org/10.1016/j.ceramint.2025.07.365
Received 1 May 2025; Received in revised form 21 July 2025; Accepted 25 July 2025
Available online 26 July 2025

Sadrnezhaad et al. [14] developed a similar model for carbon oxidation, incorporating three Andreasen's distribution coefficients for MgO particle size in their samples, and reported the kinetic parameters, including the diffusion coefficients for gases through the decarburized porous layer and the magnesia grains. They also reported the activation energies for the different steps of the kinetic process. They concluded that the diffusion of gaseous species through the decarburized porous layer had the lowest activation energy amongst the oxidation steps. Volkova et al. [15] studied oxidation kinetics in MgO-C refractory samples with 7 and 14 wt% carbon under isothermal and non-isothermal conditions across 800–1600 °C (the effect of antioxidants in the samples and models was also not considered). Liu et al. [16] examined the effect of C content on the oxidation resistance of Al-antioxidant containing MgO-C refractories. Lee et al. [17] studied MgO-C refractory degradation kinetics at 1700 °C under an Ar atmosphere, employing a shrinking core model. Hino and Takahashi [18] explored the effects of MgO and graphite flake particle size distribution on MgO-C reactions. By modifying an unreacted core model with a statistical distribution function, they predicted the mass loss in samples as a function of MgO grain size.

In their study of the slag resistance mechanisms of MgO-$MgSiO_4$-SiC-C refractories, Qi et al. [19] compared the corrosion resistance of these refractories with that of MgO-SiC-C refractories. Although the primary focus of their study was on slag corrosion phenomena, they mentioned a debonding effect between the refractory matrix and the aggregates (i.e., fused MgO in this case), which contributed to the formation of pores, debonding, and cracks. These pores facilitated deeper slag penetration, making corrosion more pronounced in the MgO–SiC–C samples. They also argued that the greater thermal expansion mismatch between the matrix and the fused MgO grains in the MgO-SiC-C refractories amplified the corrosion phenomena.

One of the shortcomings of the lab scale work is that it cannot replicate the dynamic and versatile operating environment of refractories in real settings, such as a steel EAF. Specifically, variations in oxygen partial pressure, dynamic temperature gradients, and thermal cycling on the refractory degradation are not properly captured in controlled lab conditions. Additionally, most studies focus on isolated variables and do not consider the complex interactions between multiple factors contributing to refractory degradation. The existing models on the oxidation kinetics of MgO-C refractories did not describe the role of antioxidants in the oxidation process. The effects of antioxidants and their participation in chemical reactions have not been sufficiently explored. While some studies measure pore volume fraction of the samples before and after oxidation tests (*e.g.*, using Archimedes or mercury porosimetry) [6,19–21], there is a lack of investigation into the detailed structure and morphology of the gaps and the pore network. This is especially relevant for gas permeation during oxidation, as conventional porosimetry methods, while providing accurate measurements of apparent porosity and pore size distribution, cannot offer any information about the three-dimensional structure of the porous network. The effect of MgO particle size on porous network development has also not been sufficiently explored.

These gaps hinder a full understanding of how the refractory's microstructure influences its performance and degradation. The current work builds upon previous research by consolidating existing knowledge and generating data from real samples taken from the heat-affected sidewalls of a steel EAF. This is the first study to examine samples from real operating conditions, looking into the detailed structure and morphology of the porous network. The aim is to consider the effects of multiple concurrent process variables and variations in the refractory's properties, ensuring a comprehensive capture of thermo-chemical, physical, and mechanical phenomena that can occur within the refractory in a real-world setting. The degradation mechanisms of MgO-C refractories are revisited, essential for optimizing design. In this study, the terms "pores," "gaps," "debonding," and "cracks" are used collectively to refer to any discontinuity in the solid matrix. Despite differences in their definitions, they are treated equivalently for the purpose of measuring overall porosity volume.

2. Materials and Methodology

The MgO-C refractories at the end of their lifetime were collected from the critical damage zones of a 35-ton EAF's sidewalls after more than 700 h of service in the process. During this time, the critical areas near the electrodes, as depicted in Fig. 1, sustain the most severe damage, losing about 75 % of their original thickness profile. These samples did not contact the slag or liquid steel during their service and showed no signs of skull buildup on their exposed surfaces. Additionally, unprocessed refractory samples were characterized and served as reference materials. Table I provides an overview of the chemical and physical properties of the unprocessed refractories.

The samples were microstructurally characterized using optical imaging, scanning electron microscopy with energy dispersive spectroscopy (SEM-EDS), and X-ray tomography. Macroscopic images of refractory samples were also captured using a Keyence VR 5200 surface analyzer 2D optical imaging module. The microstructural characterizations of the refractory samples were carried out using a Hitachi TM3000 SEM equipped with a Bruker XFlash®430H EDS detector. Backscattered electron (BSE) imaging and EDS data acquisition were performed with an electron acceleration voltage of 15 kV. X-ray tomography of the refractory samples was carried out by a NIKON XTH micro-CT machine with 180 kV acceleration voltage, producing a 20 μm voxel size image stack. Tomography data was processed and rendered in 3D using Comet Dragonfly software. Thermochemical calculations were also performed using FactSage™ v8.2 and its databases FactPS and FToxid [22] to complete our understanding of the solid/liquid/gas chemical reactions and their extent in the system of study.

2.1. X-ray tomography

X-ray tomography enables the study of pore interconnectivity, MgO particle size distribution, and carbon matrix damage without destructive cross-section preparation. This is critical, as conventional sectioning could alter the damaged structure and affect results obtained for pore distribution and volume fraction across the refractory depth. Additionally, in conventional microscopy, only a 1 μm surface layer of each cross-sectional area can be analyzed at a time, necessitating the examination of multiple cross sections to obtain a representative view of the damaged structure. On the other hand, tomography cannot achieve the same resolution as SEM at high magnifications. The voxel size in the analysis was 8×10^3 μm^3. Thus, the pores with a thickness of less than 20 μm were not discernible from the matrix during the data segmentation. To enhance analysis and segmentation, tomography images were processed using an 'Unsharp' filter for edge sharpening, a 'Gaussian' filter for noise reduction, and a 'Sobel' filter for edge detection. Measurement of the pore widths was conducted through manual annotation of the widths of the corresponding pores for each grain based on the three existing observation planes (XY, XZ, and ZY). Each of the pore channels was annotated at 40 locations on the observation planes close to the center of gravity of the MgO grains. For the microstructural analysis, the cross-sectional surface of the refractory was prepared for microscopy via a conventional ceramographic route consisting of sectioning, mounting in cold resin, grinding and fine polishing with 1 μm oil-based diamond suspension. Additional information can be found in previous work [23].

3. Results

3.1. Macroscopic and microstructural characterization

3.1.1. Unprocessed samples

Studying the unprocessed refractory serves as a baseline for comparison, providing valuable reference data to assess the changes and degradation that occur during the processing of the material.

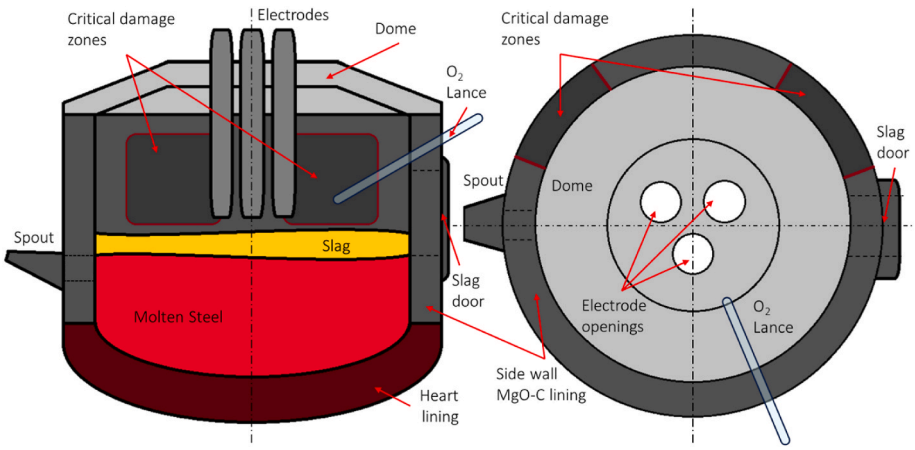

Fig. 1. Schematics of an EAF and the critical damage zones on the wall linings from where the samples were collected.

Table 1
Physicochemical properties of MgO-C refractories.

Chemical composition		
MgO grains		80.0 %
	MgO	98.0 %
	SiO_2	0.40 %
	CaO	0.75 %
	Al_2O_3	0.35 %
	Fe_2O_3	0.30 %
Residual carbon (wt%)		18.0 %
Al		2.0 %
Physical properties		
Bulk density (g/cm^3)		3.02
Apparent porosity (vol%)		3.0–5.0

Macroscopic imaging of unprocessed samples was performed to provide a broader view of the MgO-C refractory to observe its overall structure and large features that may not be apparent in microscopic analysis. Fig. 2 presents the macroscopic structural features of the unprocessed refractory samples, as acquired from the Keyence VR 5200 surface analyzer in 2D optical imaging mode. The MgO grains and metallic antioxidants are embedded within the graphite matrix. The particle size distribution of the metallic Al antioxidants varies widely, from a few microns (the smallest discernible particles) to over 2 mm. In the samples, both fine Al powder particles and aggregated Al particles were identified, and the term 'particle' was used to include both the individual fine powder particles and the larger aggregates.

The back-scattered electron (BSE) images of the unprocessed refractories, presented in Fig. 3, reveal MgO grains ranging in size from a few microns to approximately 5 mm. Examples of both fine Al powder and aggregated particles are also visible in Fig. 3. Particle size analysis of the MgO grains through tomography, illustrated in Fig. 4, also confirms these observations.

MgO grains, particularly the sintered ones, as seen in Fig. 3, may contain impurities, mainly CaO-SiO_2, that tend to segregate at the grain boundaries between original grains. Depending on their composition, these impurities can compromise the integrity of the refractory under certain service conditions. Chemical composition analysis of 52 MgO grains and their binder contents was performed using EDS, with the impurity content and the CaO/SiO_2 mass ratio detailed in Fig. 5. As shown in Figs. 5a and 42 % of the analyzed MgO grains contained less than 5 wt% total impurities, 49 % had between 5 and 15 wt% impurities, and 9 % contained more than 15 wt% impurities. These impurities were primarily composed of CaO, SiO_2, Fe_2O_3, and Cr_2O_3, with minor amounts of MnO, TiO_2, and V_2O_5 in some cases. The distribution of the CaO/SiO_2 mass ratio in the binder phase of the MgO grains is illustrated in Fig. 5b. Approximately 56 % of the MgO grains had a CaO/SiO_2 mass ratio more than 1.3, while 27 % exhibited a ratio within the range of 0.5–1.3, and the remaining grains had a ratio below 0.5.

3.1.2. *Processed samples*

The processed MgO-C refractory was segmented into several blocks, spanning from the hot face to the cold face. The "hot face" refers to the side of the refractory directly exposed to the furnace atmospheric gas, while the "cold face" refers to the bulk of the refractory, located away from the hot face. The "middle zone" represents the region between the hot and cold faces. Fig. 6 shows BSE images of processed MgO-C refractory samples from the hot face. Fig. 6a and b illustrate damage to the carbon matrix and pits formed from the detachment of relatively coarse MgO grains, indicating interfacial debonding between MgO and C. Fig. 6c reveals that the damage to the carbon structure is not uniform around all MgO grains. Pore channels were observed within the first ~75 mm of the refractory, extending from the hot face into the bulk of the material. The prevalence of these pore channels decreases further from the hot face, supporting the tomography results presented in Section 3.2. Fig. 6d shows a MgO grain located near the hot face, with fine

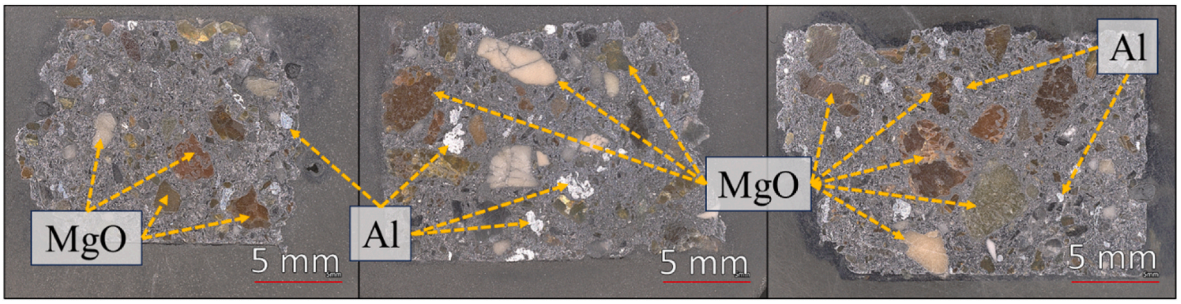

Fig. 2. Optical surface images from unprocessed refractory samples.

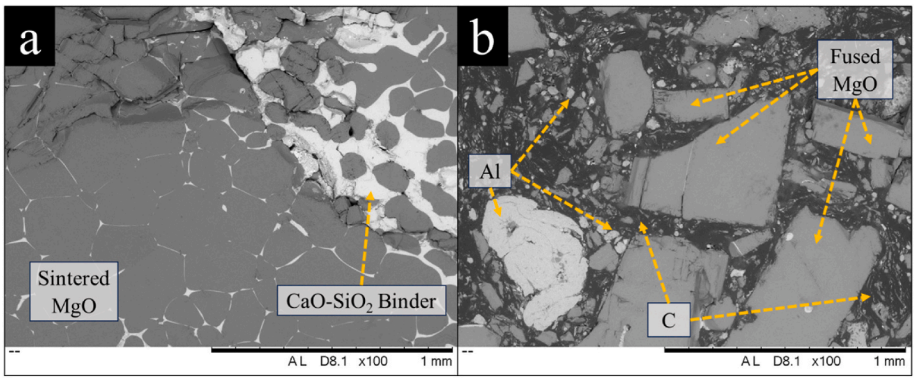

Fig. 3. BSE micro-images of the unprocessed refractory: a) sintered MgO grain containing CaO-SiO_2 impurities, and b) fused MgO grains and Al particle distribution in the carbon matrix.

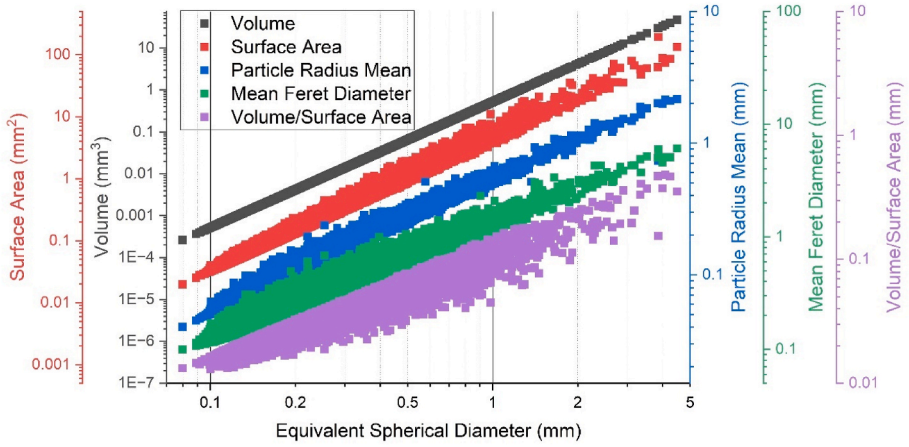

Fig. 4. MgO particle size analysis, tomography results of unprocessed samples.

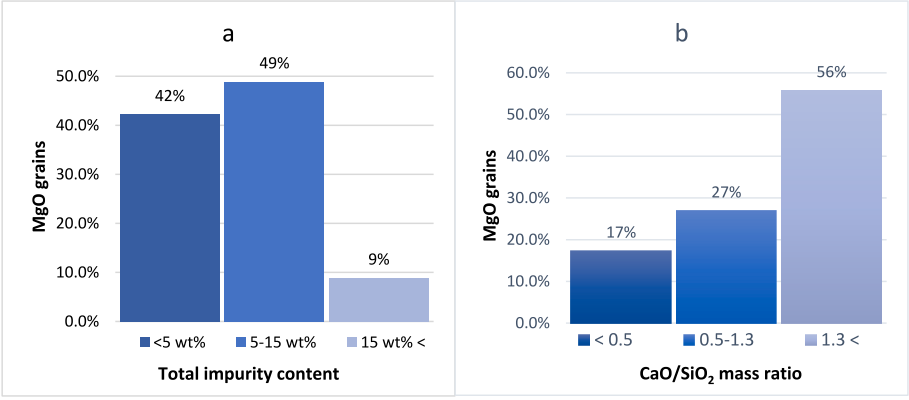

Fig. 5. Chemical analysis of various MgO grains: a) total impurity content, and b) CaO/SiO_2 ratio in binder phase.

metallic Fe particles accumulating along MgO grain boundaries. This phenomenon is attributed to the reduction of iron oxide impurities to metallic Fe, facilitated by the reducing conditions in the refractory body. It was also noted that MgO had dissolved into the CaO-SiO_2 binder phase, where the CaO/SiO_2 ratio of the binder was measured to be 0.72 (in the case of the example in Fig. 6d), which is associated with the solubility limit of MgO in the low-temperature liquids formed from these binder phases.

Fig. 7 shows two examples of partially oxidized Al grain within the carbon matrix at the hot face of the processed refractory, along with corresponding EDS elemental maps. The analysis revealed that the outer shell of the Al grain is oxidized, while its core remains metallic and unreacted. This behavior was consistently observed in the processed samples, particularly for Al particles larger than 200 μm. Such layered oxidation highlights the incomplete reaction of large Al grains under the given processing conditions. Supporting microscopy data were collected from over ten distinct regions across two identical sample sets; each set comprising three pieces taken from the hot face down to approximately 6~7 cm deep into the refractory body. Each sample piece had an observable surface area of about 3 cm^2, and in total, six sample pieces were investigated. Although micrographs illustrating representative features were captured, a comprehensive statistical analysis was not

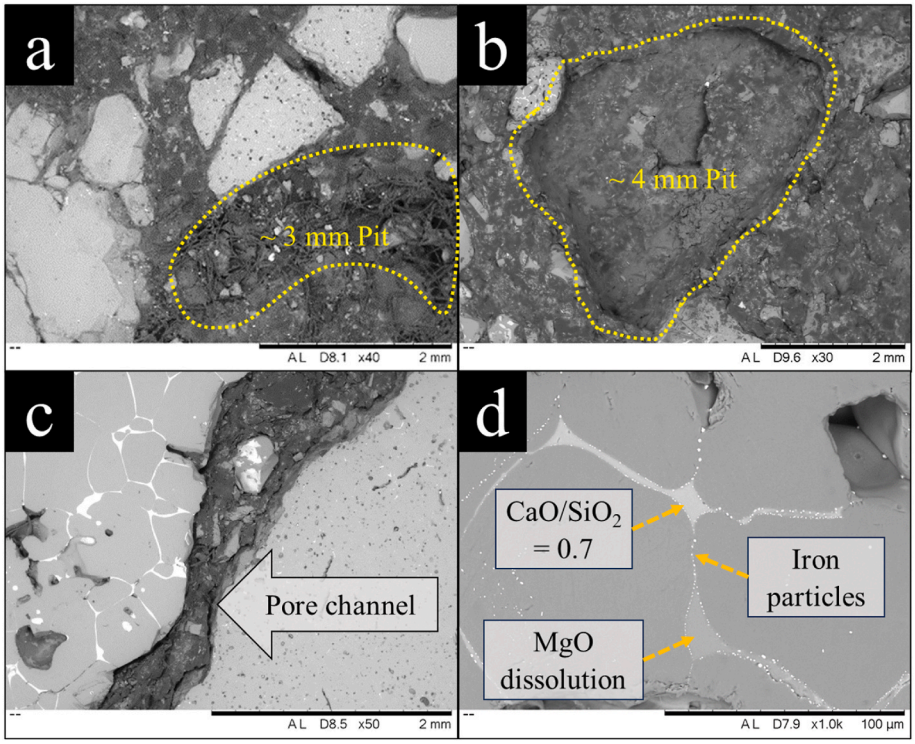

Fig. 6. BSE micro-images of processed MgO-C refractory samples from the hot face: a and b) deterioration of the carbon matrix and remaining pits from detached grains; c) formation of pore channels around MgO grains; and d) precipitation of metallic Fe on the MgO crystallite boundaries and partial dissolution of MgO in the binder phase.

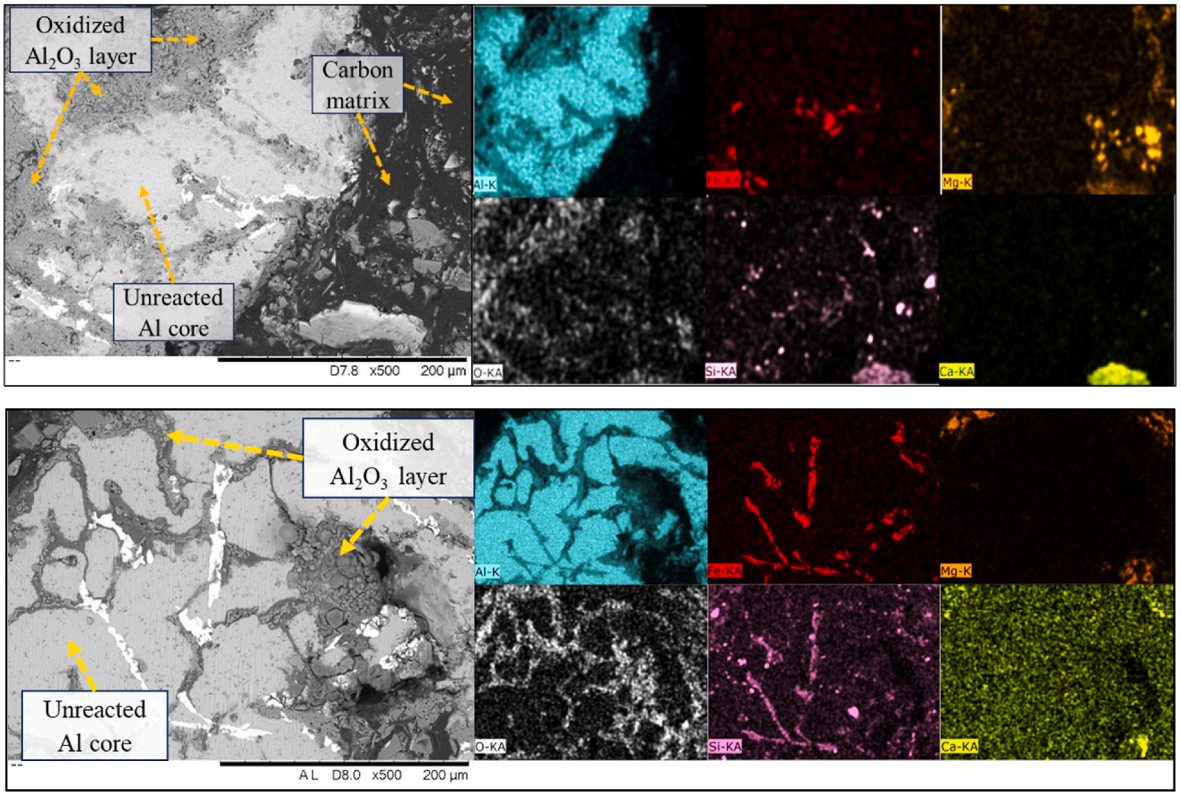

Fig. 7. Examples of partial oxidation of Al aggregated grains within the carbon matrix at the hot face of the processed refractory.

conducted, as it falls outside the scope and focus of this study.

3.2. Analysis of pore volume fraction and network morphology

Several microstructural changes were observed comparing the processed MgO-C refractory with the unprocessed samples, including the development of pore channels around the MgO grains, dissolution of the MgO grains in the binder phase across the grain boundaries, and partial oxidation of large Al deoxidant grains. The potential impact of the two latter factors on the integrity of the refractory is discussed in Section 4.3. The extent of pore channel development is of particular concern, as these refractories are vulnerable to oxidation. The interconnectivity and volume of the pore channels, developed predominantly in the MgO-C refractories, could not be fully analyzed using SEM. Therefore, 3D tomography was employed to further investigate these features. Fig. 8 illustrates the 3D tomography of the developed pore structure in the processed (hot face to cold face) and unprocessed samples. The acquired data were segmented based on X-ray absorption, and the transparency of the segmented regions was adjusted to highlight the pore network. Specifically, the carbon matrix and MgO grains were rendered completely transparent, while the pores were kept visible for investigation. Fig. 8a clearly shows that the sample adjacent to the exposed hot face of the refractory (PM.01), which contains an interconnected network of pore channels with wider gaps compared to the following samples: Fig. 8b, the second zone (PM.02); and Fig. 8c, the third zone (PM.03). These samples are located deeper within the refractory, up to approximately 7.5 cm into its body. The same trend of behavior was observed in the next samples as the analysis moved toward the cold face of the refractory. Fig. 8d shows the pore analysis of an unprocessed refractory as a reference for the analysis.

Pore volume fraction in each sample piece was measured by 3D image analysis methods via counting the total number of voxels in the selected volume and the number of voxels from the segmented pores. Fig. 9 depicts the pore volume fraction within the MgO-C refractory body as a function of distance from the cold zone (from left to right). The graph demonstrates that the pore volume fraction increases from 0.3 to 6 vol% as the distance from the cold face increases in the refractory, and we get closer to the hot face. A quadratic polynomial fit to the data indicates a clear trend, revealing that the rate of pore volume development rises as the distance from the cold face toward the hot face increases. Considering the deterioration and reduction in thickness of the refractory from the hot face, extrapolating the pore volume fraction beyond this point suggests a pore content of approximately 10 vol%. At this level, the pore content is likely to compromise the refractory's structural integrity significantly, potentially resulting in collapse at the hot face.

3.3. Analysis of pore channel width

The tomography images from the processed refractory were segmented for quantitative analysis of pore channel widths. Fig. 10 shows the segmented microstructural images, distinguishing pores in a teal color, while the carbon matrix is dark brown (the rest are the MgO grains). The morphological alignment of the pore channels with the geometrical shapes of the MgO grains is evident, with thicker channels surrounding the larger grains. Additionally, cracks form in the matrix connecting the channels surrounding nearby large MgO grains.

The widths of the pore channels in the first sample piece (PM.01), adjacent to the hot face, were analyzed as a function of the equivalent spherical diameter around the MgO grain it surrounded. An equivalent volume sphere was selected as the measuring tool for the particle size analysis of the MgO grains in the sample. The volume of the grains was calculated based on the number of voxels contained within each segmented grain. Fig. 11 depicts the relationship between the width of the pore channels and the equivalent spherical diameter of MgO grains larger than 2 mm. When the MgO grain size decreased below

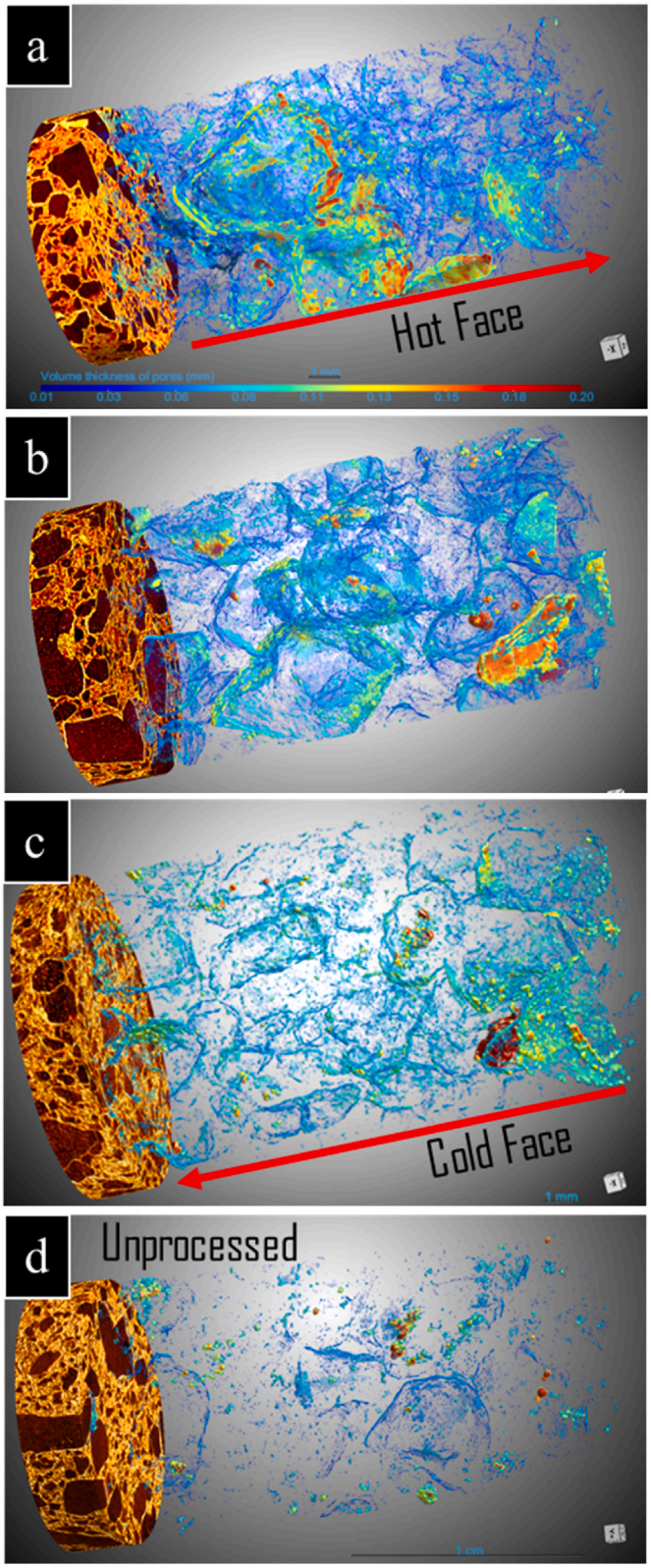

Fig. 8. 3D tomography images showing pore networks in the MgO-C refractory for processed sample: (a) zone adjacent to the hot face (PM01), (b) middle zone (PM02), (c) zone adjacent to the cold face (PM03), and (d) unprocessed sample.

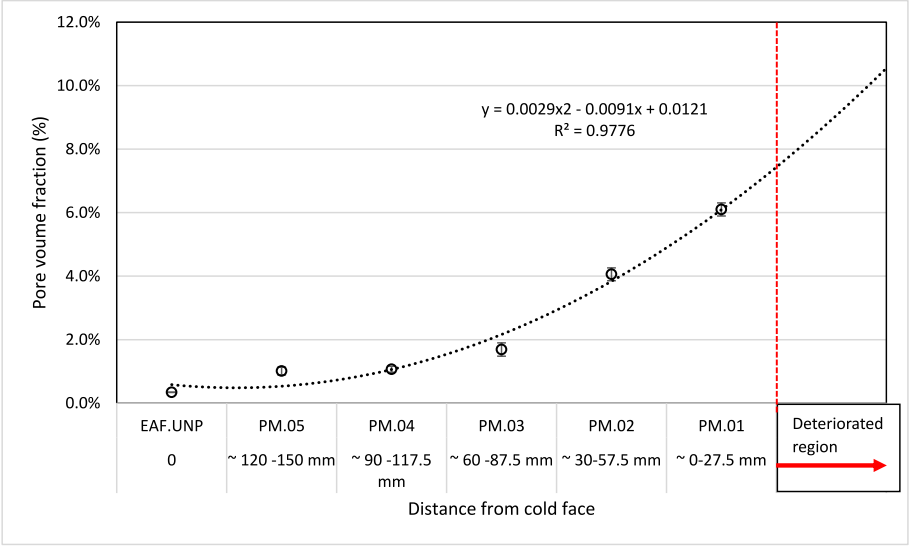

Fig. 9. Pore volume fraction versus distance from the cold face (left to right) in the processed MgO-C refractory samples.

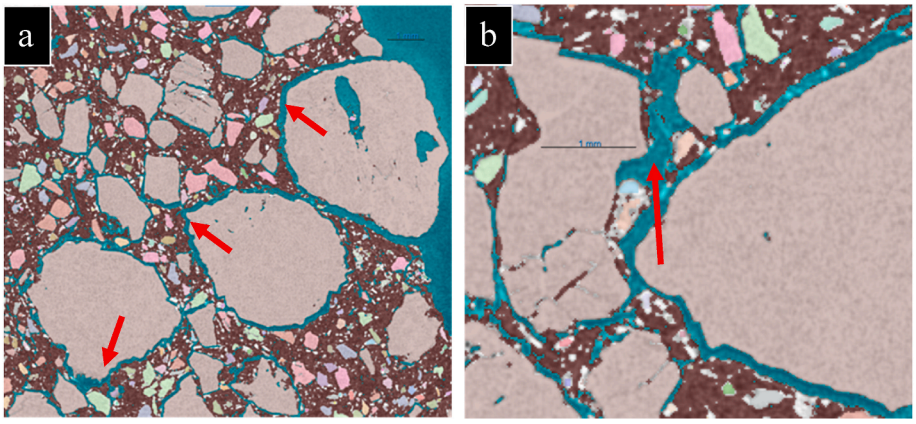

Fig. 10. Segmented microstructural images acquired via X-ray tomography for pore analysis: (a) pore channels formed around coarse MgO grains, and (b) cracks resulting from the pore channel interconnectivity.

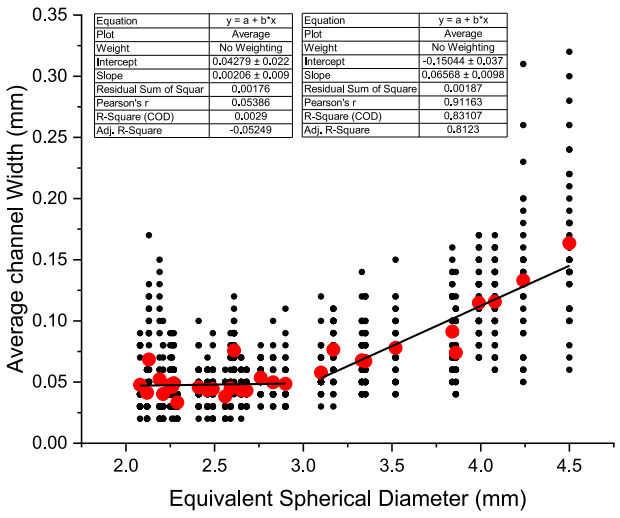

Fig. 11. Pore channel width measurements as a function of the equivalent spherical diameter of MgO grain.

approximately 2 mm, the surrounding pore widths also dropped below 20 μm, the resolution limit of the analysis (voxel size). As a result, analyzing the pores around grains smaller than 2 mm became unreliable. In Fig. 11, the small black circles represent the raw measurements, while the large red circles represent the averages of the measurements. It was noted that when the MgO equivalent spherical diameter was less than 3 mm, the average thickness of the pore channels did not considerably change with the particle size, while for the MgO grains of more than 3 mm equivalent spherical diameter, the thickness of the pore channels increased with particle size. The data was then divided into two sections, and linear regression analysis was done on the two sections of the average values of the measured pore widths. The results revealed a strong correlation between pore channel width and particle size for particles larger than 3 mm in diameter, with an adjusted R-squared value of 0.81. In contrast, for particles smaller than 3 mm, the regression slope was nearly zero, and the adjusted R-squared value was negligible, indicating no meaningful correlation. As MgO grain size increased from 3 mm to 4.5 mm, the average pore channel width rose from 0.05 mm to 0.17 mm.

4. Discussion

4.1. Thermal expansion mismatch and pore channel formation

The results showed that a considerable volume of pore channel structure developed around the MgO grains at the interface between the C matrix in the hot zone of the refractory (see Fig. 8), and that there is direct correlation between the pore channel width and the particle size of the MgO grains (see Fig. 11). That is, with increasing MgO grain size, the pore channels around them widen. The size of the remaining pits caused by the detachment of MgO grains during microscopy sample preparation further confirmed this, as MgO grains as large as 3–4 mm was found to have detached from the carbon matrix, leaving pits behind (see Fig. 6). Additionally, the formation of cracks and gaps in the matrix between large MgO grains was also evident (see Fig. 10). Our observations are in agreement that the extent of interfacial debonding and deterioration around the coarser MgO particles was significant in comparison to the fine MgO grains.

Qi et al. [24] previously noted that the mismatch in thermal expansion coefficients between the matrix and the grains could lead to interface debonding, although the details were not investigated. Moreover, it has been previously established that the thermal expansion mismatch between the matrix and the reinforcement particles can lead to the formation of debonding and cracks in the matrix in intermetallic composite materials [25].

The thermal expansion coefficients of MgO and graphitic carbon are given in Table II [26,27]. It is well established that the linear thermal expansion coefficient (α_T) of graphite varies significantly with crystallographic orientation and differs markedly from that of MgO grains. Xu et al. [28] measured the overall α_T of an MgO-C refractory composed of 83 wt% MgO and 12 wt% flake graphite to be 10.0×10^{-6} °C^{-1} at 1400 °C while, the α_T of MgO is reported to be approximately 15×10^{-6} °C^{-1}. As a result, the average α_T of the carbon matrix can be approximated at $\sim 5 \times 10^{-6}$ °C^{-1}, a value closer to the in-plane expansion coefficient of graphite. This indicates a substantial thermal expansion mismatch between MgO and the carbon matrix. Such a mismatch promotes the formation of pore channels around MgO grains during thermal cycling, contributing to microstructural degradation.

Additionally, the effect of thermal expansion mismatch between the matrix and grains is further enhanced by the volume of the MgO grains. The extent of volume expansion for MgO aggregates becomes more important as the initial grain size increases. This explains why pore network development is more pronounced around larger grains, as observed in the tomography analysis (see Fig. 11). Assuming a 3D expansion for MgO, the volume expansion follows Equation (1):

$$\Delta V = V_o \, \alpha_V \, \Delta T \tag{1}$$

where ΔV is the change in volume of MgO grain, V_o is the initial volume, and α_V is the coefficient of volume expansion. Note that for isotropic solids, α_V is approximately equal to $3\alpha_T$. Moreover, the thermal expansion mismatch amplifies stress-induced debonding at the MgO-C interface. A significant thermal expansion mismatch within a composite material can generate stress cycles due to temperature fluctuations, leading to crack formation. This phenomenon, known as 'thermal fatigue,' occurs as damage accumulates over repeated heating and cooling cycles, causing cracks to initiate and propagate at the interfaces between material phases with differing thermal expansion coefficients. Lu et al. [25] reported a non-dimensional group ($\mathscr{R}$) called the magnitude of cracking coefficient, for assessing the crack formation, Equation (2):

$$\mathscr{R} = R(E_m \epsilon_T / K_m)^2 \tag{2}$$

where R is the particle size, K_m the matrix toughness, E_m the matrix elastic modulus, and ϵ_T the misfit strain, given by Equation (3):

$$\epsilon_T = \int_{T_0}^{T} \Delta\alpha_T dT \tag{3}$$

with $\Delta\alpha_T$ being the difference between the linear thermal expansion coefficient of the aggregate and the matrix. The cracking can be prevented if $\mathscr{R}$ is below a critical value ($\mathscr{R}c$), which depends on the MgO grain volume fraction, their aspect ratio, and the ratio of the elastic modulus of the reinforcement to the matrix, and the friction coefficient at the matrix-grain interface. The ($\mathscr{R}c$) can be determined experimentally as a part of the continuation of this work in the future.

These expressions help to qualitatively explain the observed damage mechanisms. As seen in Equation (3), the misfit strain ϵ_T increases with the thermal expansion mismatch $\Delta\alpha_T$ and the temperature range ΔT. This strain directly influences the stress developed at the particle-matrix interface, as seen in Equation (2), where a higher ϵ_T or matrix stiffness E_m increases the cracking coefficient $\mathscr{R}$. Consequently, for a given matrix toughness K_m, coarser MgO grains are more likely to exceed the critical radius R_C, promoting interfacial debonding and pore channel formation. This aligns with our experimental observations that larger MgO grains are surrounded by wider pore channels and are more prone to detachment, as illustrated in Figs. 6, 8 and 11. Although a quantitative application of these models is planned in future work, the current findings qualitatively support the idea that thermal expansion mismatch—amplified by increasing MgO grain size—is a key driver in the development of microstructural degradation.

Table 2
Thermal expansion coefficient of MgO and graphite from the literature.

	Expansion behavior	α_T ($°C^{-1}$)	T	Ref.
MgO	Isotropic	10.4×10^{-6}	300 K	[26]
		17.5×10^{-6}	2000 K	
Graphite	Anisotropic			
	In-plane	-1.5×10^{-6}	300 K	[27]
		1.2×10^{-6}	2000 K	
	Out-of-plane	$\sim 27 \times 10^{-6}$	300 K	
		$\sim 35 \times 10^{-6}$	2000 K	

4.2. Deterioration mechanisms

The vulnerability of refractories to oxidation, particularly carbon oxidation, has been a major focus of previous lab research work, and has been mentioned as the primary cause of deterioration [6,8,9,14,15,17,29]. The C oxidation is primarily driven by a series of chemical reactions, given in equations (4)–(6):

$$2C_{(s)} + O_{2(g)} = 2CO_{(g)}; \Delta G^\circ = -223,426 - 175.30T \tag{4}$$

$$2CO_{(g)} \rightleftharpoons CO_{2(g)} + C_{(s)}; \Delta G^\circ = -170,707 + 174.46T \tag{5}$$

$$C_{(s)} + MgO_{(s)} = CO_{(g)} + Mg_{(g)}; \Delta G^\circ = 648,101 + 30.84T \log T - 404.38T \tag{6}$$

Reaction (Eq. (4)) is the direct oxidation of carbon, reaction (Eq. (5)) is reversible Boudouard's reaction, and reaction (Eq. (6)) is known as the indirect oxidation of carbon by MgO grains or simply MgO-C self-reaction.

If pore channel formation in the refractory body were primarily driven by the solid-state MgO–C chemical reaction (i.e., decarburization), a higher reaction extent would be expected around finer MgO aggregates. Their smaller volume yields a higher specific surface area, thereby increasing the available solid–solid reaction interface, as suggested by fundamental reaction kinetics [18,30]. Supporting this, Hino et al. [18] reported that reducing MgO particle size in MgO–C samples led to an increased mass loss during oxidation tests. However, their model overestimated the mass loss in fine-grained samples, which they attributed to the sintering of fine MgO particles at elevated

temperatures, effectively increasing the apparent grain diameter. In contrast, our investigation of MgO–C refractories from an actual electric arc furnace (EAF) steelmaking process, specifically, from the radiation-affected heat walls, indicated that major pore channel formation, cracking, and disintegration predominantly occur at the interface between coarse MgO grains and the surrounding carbon matrix. This behavior is strongly influenced by the thermal expansion mismatch between MgO and C. Coarser MgO grains undergo greater volumetric expansion (Eq. (1)), leading to more pronounced debonding at the interface, which increases internal stress and contributes to crack initiation and structural failure.

The degradation mechanism of MgO-C refractories is more complex than merely being attributed to carbon oxidation alone [17]. In addition to simultaneous diffusion of O_2 inward through the decarburized passages and C-O_2 chemical reaction and MgO-C self-reaction (activated at above 1400 °C [6]), there are parallel thermally activated physical and mechanical phenomena including the thermal expansion mismatch and crack initiation and propagation under thermal cycle that provide the path for O_2 further diffusion and direct C oxidation (Eq. (4)). Therefore, the degradation mechanism of MgO-C refractory can be revised as follows: (1) direct C oxidation in contact with the oxidizing atmosphere; (2) MgO-C self-reaction (amplified by fine MgO grains); (3) thermal expansion mismatch (amplified by coarse MgO grains); and (4) crack formation. All of the mentioned mechanisms could provide pathways for O_2 diffusion into the refractory and accelerate the C oxidation. In addition, the mechanisms (3) and (4) contribute in parallel to the disintegration of the refractory. The extent of each contribution to the refractory deterioration cannot yet be identified. Fig. 12 summarizes the overall degradation mechanisms in the MgO-C refractories from radiation-affected side-walls of the EAF based on both microstructural characterization and theoretical knowledge.

4.3. Additional minor detrimental phenomena

In addition to the primary degradation mechanisms, localized melting and partial dissolution of MgO grains into the CaO–SiO_2 binder

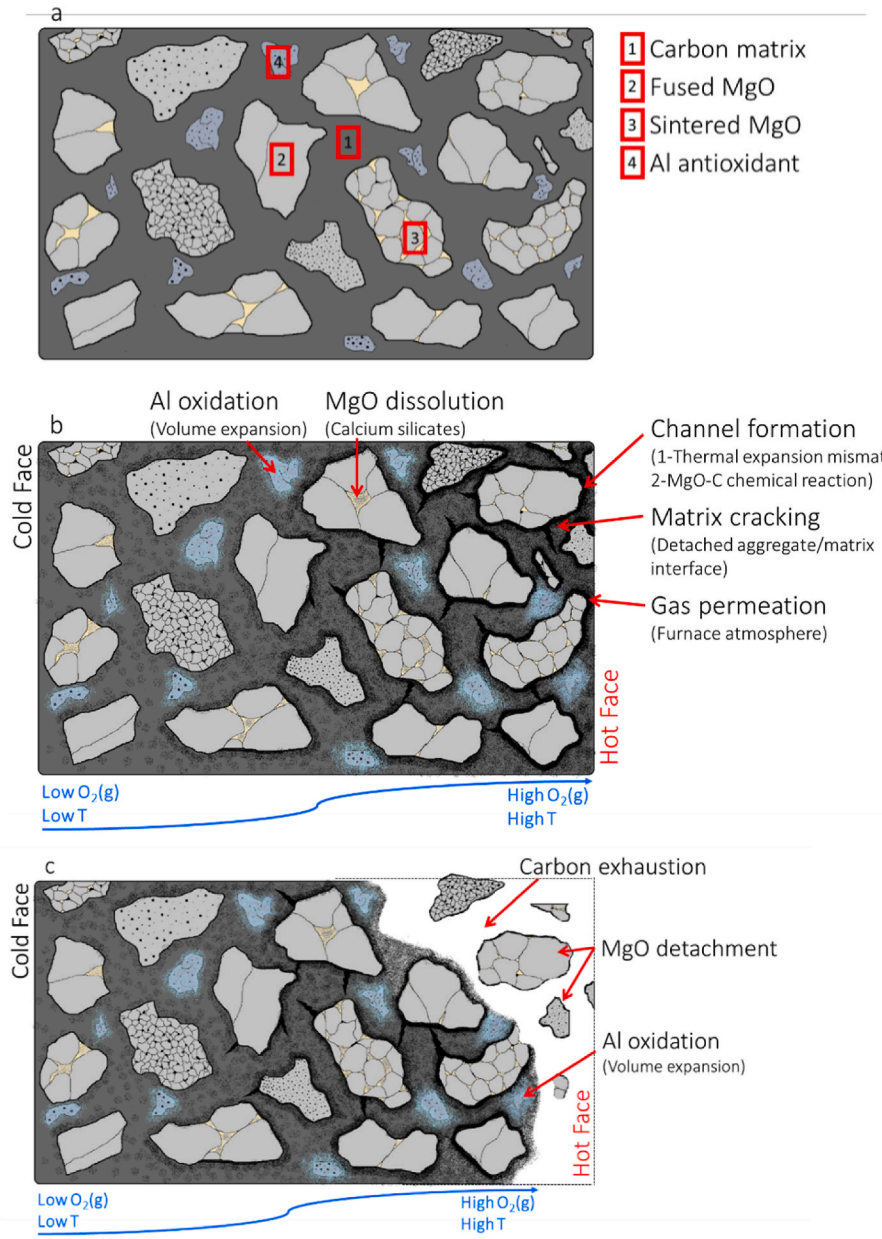

Fig. 12. Schematic representation of a) the unprocessed MgO-C refractory, b) the most notable deterioration mechanisms, and c) the refractory after deterioration.

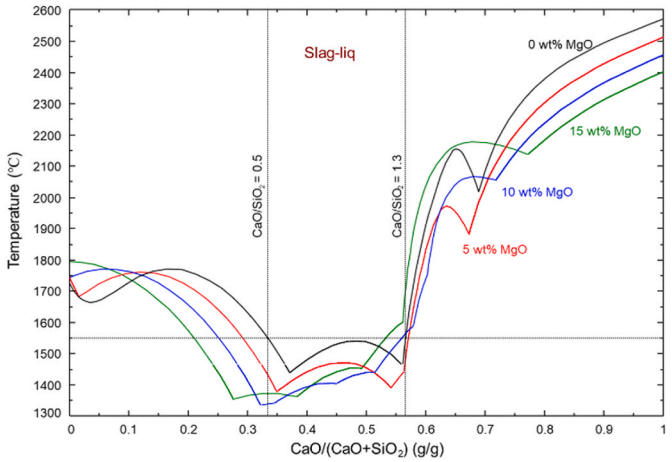

Fig. 13. Calculated liquidus temperatures of the CaO-SiO_2 binder phases. The effect of MgO concentrations (5–15 w%) on the liquidus temperatures is also shown.

phase were observed. As shown in Fig. 13, the melting point of the binder phase decreases sharply to below the average EAF operating temperature (~1550 °C) when the CaO/SiO_2 mass ratio falls between 0.5 and 1.3. According to Fig. 5b, only 27 % of the analyzed MgO grains exhibited a binder with a CaO/SiO_2 ratio within this range. Given the limited total content of the binder phase within MgO aggregates (see Table I) and the lack of direct contact with liquid slag to amplify the dissolution phenomena, this effect is considered minor compared to the dominant influence of pore network development.

Oxidation resistance in MgO-C refractories is enhanced through the addition of metallic antioxidants, particularly Al. Aluminium participates in a series of reactions forming intermediate carbides (Al_4C_3) and/or nitrides (AlN), and subsequently oxides (Al_2O_3) and spinel ($MgAl_2O_4$), contributing to improved resistance by sealing pores and reducing oxygen ingress [5,31,32]. However, SEM-EDS analysis (as seen in Fig. 7) revealed that Al particles larger than 200 μm tend to develop dense surface oxide layers, which hinder complete oxidation and reduce their effectiveness. Optimizing antioxidant particle size distribution could enhance their efficiency and improve refractory lifespan.

5. Conclusions

The present study analyzed and revised the degradation mechanisms of MgO-C refractories from radiation-affected walls of a steel EAF, which is crucial for enhancing sustainability in steelmaking, especially with the growing demand for EAFs in future green steel production. This work highlights the critical role of pore network development in the degradation of MgO-C refractories in real industrial settings. The most important findings are summarized below:

- X-ray tomography and SEM-EDS analysis revealed that the thermal expansion mismatch between MgO grains and the carbon binder plays a critical role in refractory degradation. This mismatch leads to crack formation, increased oxygen permeability from the furnace atmosphere, and subsequent oxidation of the carbon matrix. Coarser MgO grains worsen this effect by creating larger, interconnected pore channels that accelerate degradation. Linear regression analysis confirmed that coarser MgO grains (>3 mm) were linked to wider pore channels and faster degradation. Limiting the maximum MgO grain size could help reduce debonding, thermal stress-induced cracking, and oxidation-driven deterioration.
- Thermophysical, thermo-mechanical, and thermochemical phenomena collectively contribute to the disintegration of MgO-C refractories. The degradation mechanisms proposed in the previous work can be expanded to include: (1) direct oxidation of carbon in contact with the oxidizing atmosphere; (2) the MgO-C self-reaction, particularly pronounced with finer MgO grains; (3) thermal expansion mismatch between MgO and carbon, which is more severe with coarser MgO grains; and (4) crack formation and the eventual disintegration driven by these combined effects.
- Optimizing the particle size distribution of antioxidants may improve their effectiveness in preventing premature oxidation. In this study, metallic Al particles exceeding 200 μm were observed to be suboptimal, as their protective oxide shells inhibited full participation in oxidation reactions.

As a final note, the authors would recommend future studies to explore alternative bonding strategies, nanostructured reinforcements, and modified carbon matrices to improve refractory durability and performance under industrial conditions.

CRediT authorship contribution statement

Kianoosh Kaveh: Writing – original draft, Visualization, Software, Methodology, Investigation, Formal analysis. **Mansoor Barati:** Writing – review & editing, Validation, Resources. **Mohammad Jahazi:** Writing – review & editing, Supervision, Resources, Project administration, Funding acquisition, Conceptualization. **Elmira Moosavi-Khoonsari:** Writing – review & editing, Validation, Supervision, Resources, Project administration, Funding acquisition, Conceptualization.

Declaration of competing interest

The authors declare that they have no known competing financial interests or personal relationships that could have appeared to influence the work reported in this paper.

Acknowledgement

The authors would like to acknowledge Finkl Steel-Sorel and Mitacs Accelerate Program (IT28458) for financial support of the project. In addition, the authors highly appreciate Finkl Steel-Sorel, especially Paloma Isabel Gallego, Patrice Menard, Valentin Hurel, and Jean-Benoit Morin for providing the MgO-C refractory samples and their collaboration and support for this project.

References

[1] I.E.A. Iea, Steel Production by Share of Different Process Routes in the Net Zero Scenario, 2018-2030, IEA, Paris, 2021. IEA Website.
[2] N. Pardo, J.A. Moya, Prospective scenarios on energy efficiency and CO_2 emissions in the European iron & steel industry, Energy 54 (2013) 113–128.
[3] M. Kirschen, T. Hay, T. Echterhof, Process improvements for direct reduced iron melting in the electric Arc furnace with emphasis on slag operation, Processes 9 (2) (2021) 402.
[4] J. Freuhan, The Making. *Shaping and Treating of Steel 11th Edition—Steelmaking and Refining Volume*, The AISE Steel Foundation, Pittsburgh, Pa, 1998.
[5] S. Zhang, N. Marriott, W. Lee, Thermochemistry and microstructures of MgO–C refractories containing various antioxidants, J. Eur. Ceram. Soc. 21 (8) (2001) 1037–1047.
[6] M.-A. Faghihi-Sani, A. Yamaguchi, Oxidation kinetics of MgO–C refractory bricks, Ceram. Int. 28 (8) (2002) 835–839.
[7] E.M.M. Ewais, Carbon based refractories, J. Ceram. Soc. Jpn. 112 (1310) (2004) 517–532.
[8] K.S. Campos, et al., The influence of B_4C and MgB_2 additions on the behavior of MgO–C bricks, Ceram. Int. 38 (7) (2012) 5661–5667.
[9] S. Gao, et al., Effect of Fe addition on the microstructure and oxidation behavior of MgO–C refractory, Mater. Chem. Phys. 238 (2019) 121935.
[10] Y. Yang, et al., Cr_7C_3: a potential antioxidant for low carbon MgO–C refractories, Ceram. Int. 46 (12) (2020) 19743–19751.
[11] Z. Liu, et al., Comparative study of B_4C, $Mg_2B_2O_5$, and ZrB_2 powder additions on the mechanical properties, oxidation, and slag corrosion resistance of MgO–C refractories, Ceram. Int. 48 (10) (2022) 14117–14126.
[12] T. Zhang, et al., Elucidating the role of Ti_3AlC_2 and Ti_3SiC_2 in oxidation mechanisms of MgO–C refractories, Ceram. Int. 49 (7) (2023) 11257–11265.

[13] S. Nanda, et al., Raw materials, microstructure, and properties of MgO–C refractories: directions for refractory recipe development, J. Eur. Ceram. Soc. 43 (1) (2023) 14–36.
[14] S. Sadrnezhaad, et al., Oxidation mechanism of C in MgO–C refractory bricks, J. Am. Ceram. Soc. 89 (4) (2006) 1308–1316.
[15] O. Volkova, P.R. Scheller, B. Lychatz, Kinetics and thermodynamics of carbon isothermal and non-isothermal oxidation in MgO-C refractory with different air flow, Metall. Mater. Trans. B 45 (5) (2014) 1782–1792.
[16] Z. Liu, et al., Oxidation resistance and wetting behavior of MgO-C refractories: effect of carbon content, Materials 11 (6) (2018) 883.
[17] J. Lee, J. Myung, Y. Chung, Degradation kinetics of MgO-C refractory at high temperature, Metall. Mater. Trans. B 52 (3) (2021) 1179–1185.
[18] Y. Hino, K. Takahashi, Effects of particle size distribution of MgO and carbon on MgO–C reaction behaviour, ISIJ Int. 62 (9) (2022) 1836–1844.
[19] B. Hashemi, Z. Nemati, M. Faghihi-Sani, Effects of resin and graphite content on density and oxidation behavior of MgO-C refractory bricks, Ceram. Int. 32 (3) (2006) 313–319.
[20] S. Mahato, S.K. Behera, Oxidation resistance and microstructural evolution in MgO–C refractories with expanded graphite, Ceram. Int. 42 (6) (2016) 7611–7619.
[21] J. Xiao, et al., Oxidation behaviors of MgO-C refractories with different Si/SiC ratio in the 1100–1500 C range, Ceram. Int. 45 (17) (2019) 21099–21107.
[22] C.W. Bale, et al., FactSage thermochemical software and databases, Calphad 26 (2) (2002) 189–228.
[23] K. Kaveh, et al., Post-Mortem Study of magnesia-carbon Refractory Bricks Exposed to Thermal Radiation in Electric Arc Furnace Steelmaking, Association for Iron & Steel Technology, 2022.
[24] X. Qi, et al., Slag resistance mechanism of MgO–Mg_2SiO_4–SiC–C refractories containing porous multiphase aggregates, Ceram. Int. 49 (10) (2023) 15122–15132.
[25] T. Lu, et al., Matrix cracking in intermetallic composites caused by thermal expansion mismatch, Acta Metall. Mater. 39 (8) (1991) 1883–1890.
[26] A.M. Rao, K. Narender, Studies on thermophysical properties of CaO and MgO by γ-Ray attenuation, J. Thermodynam. 2014 (1) (2014) 123478.
[27] L. Zhao, et al., A review of the coefficient of thermal expansion and thermal conductivity of graphite, N. Carbon Mater. 37 (3) (2022) 544–555.
[28] X. Xu, et al., Influence of flake graphite coated MgO particles on thermal shock resistance and fracture behaviour of MgO-C refractories based on Brazilian splitting test with digital image correlation method and acoustic emission technique, Ceram. Int. 51 (5) (2025) 6458–6467.
[29] Z. Liu, et al., Effect of carbon content on the oxidation resistance and kinetics of MgO-C refractory with the addition of Al powder, Ceram. Int. 46 (3) (2020) 3091–3098.
[30] M. Soustelle, Handbook of Heterogenous Kinetics, John Wiley & Sons, 2013.
[31] T. Zhu, et al., Formation of hollow MgO-rich spinel whiskers in low carbon MgO–C refractories with Al additives, J. Eur. Ceram. Soc. 34 (16) (2014) 4425–4432.
[32] C. Atzenhofer, H. Harmuth, Phase formation in MgO-C refractories with different antioxidants, J. Eur. Ceram. Soc. 41 (14) (2021) 7330–7338.